

See discussions, stats, and author profiles for this publication at: <https://www.researchgate.net/publication/255970707>

Nanoparticle–Nanoparticle Interactions in Biological Media by 2 Atomic Force Microscopy

DATASET · AUGUST 2013

READS

44

4 AUTHORS, INCLUDING:



[Georgios Pyrgiotakis](#)

Harvard University

45 PUBLICATIONS 1,157 CITATIONS

[SEE PROFILE](#)



[Sotiris E. Pratsinis](#)

ETH Zurich

503 PUBLICATIONS 16,502 CITATIONS

[SEE PROFILE](#)



[Philip Demokritou](#)

Harvard University

109 PUBLICATIONS 1,449 CITATIONS

[SEE PROFILE](#)

Nanoparticle–Nanoparticle Interactions in Biological Media by Atomic Force Microscopy

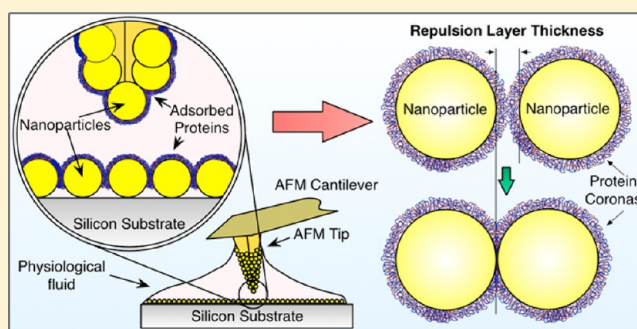
Georgios Pyrgiotakis,[†] Christoph O. Blattmann,[‡] Sotiris Pratsinis,[‡] and Philip Demokritou^{*,†}

[†]Center for Nanotechnology and Nanotoxicology at Harvard School of Public Health, Harvard University, 665 Huntington Avenue, Boston, Massachusetts 02115, United States

[‡]Particle Technology Laboratory, Institute of Process Engineering, Department of Mechanical and Process Engineering, Swiss Federal Institute of Technology Zurich (ETH Zurich), Sonneggstrasse 3, CH-8092, Zurich, Switzerland

S Supporting Information

ABSTRACT: Particle–particle interactions in physiological media are important determinants for nanoparticle fate and transport. Herein, such interactions are assessed by a novel atomic force microscopy (AFM)-based platform. Industry-relevant CeO₂, Fe₂O₃, and SiO₂ nanoparticles of various diameters were made by the flame spray pyrolysis (FSP)-based Harvard Versatile Engineering Nanomaterials Generation System (Harvard VENGENES). The nanoparticles were fully characterized structurally and morphologically, and their properties in water and biological media were also assessed. The nanoparticles were attached on AFM tips and deposited on Si substrates to measure particle–particle interactions. The corresponding force was measured in air, water, and biological media that are widely used in toxicological studies. The presented AFM-based approach can be used to assess the agglomeration potential of nanoparticles in physiological fluids. The agglomeration potential of CeO₂ nanoparticles in water and RPMI 1640 (Roswell Park Memorial Institute formulation 1640) was inversely proportional to their primary particle (PP) diameter, but for Fe₂O₃ nanoparticles, that potential is independent of PP diameter in these media. Moreover, in RPMI+10% Fetal Bovine Serum (FBS), the corona thickness and dispersibility of the CeO₂ are independent of PP diameter, while for Fe₂O₃, the corona thickness and dispersibility were inversely proportional to PP diameter. The present method can be combined with dynamic light scattering (DLS), proteomics, and computer simulations to understand the nanobio interactions, with emphasis on the agglomeration potential of nanoparticles and their transport in physiological media.



INTRODUCTION

The increasing use of nanoparticles in commercial products and industrial processes makes their environmental¹ and occupational² exposures inevitable.³ Preliminary evidence indicates the potential of nanoparticles to cross biological barriers and cause adverse health effects.⁴ On a positive note, nanoparticle-based theranostics⁵ are one of the most promising applications that can help shape the way diseases⁶ are diagnosed and treated⁷ by MRI,⁸ X-rays,⁹ and photo acoustic tomography (PAT).¹⁰ Both the potential adverse effects and the theranostics efficacy are directly related to the nanoparticle uptake from the cells. Nanoparticle–nanoparticle interactions have recently gained attention as they directly impact the cellular uptake of nanoparticles. Specifically, the adsorbed proteins on nanoparticle surfaces and the formation of the so-called protein corona have a key role in these interactions,¹¹ as they determine the nanoparticle agglomeration state, as well as their fate and transport in a biological media (mobility, settling, etc.). We recently showed that transport of nanoparticles in physiological media depends on the hydrodynamic diameter and effective density¹² of the agglomerates that are formed when nano-

particles are exposed to physiological fluids.¹³ The effective density depends largely on the interaction potential (repulsion or attraction) and the corresponding force between nanoparticles.¹¹

Because of the importance of the corona in the nanoparticle–nanoparticle interactions, many studies have focused on the identification of parameters influencing the adsorption of proteins on the surface of nanoparticles in various physiological fluids and the corresponding link to the physicochemical properties of nanoparticles.¹⁴ Differential plasma protein binding and proteomics analysis showed that the protein binding depends on PP diameter, shape, and charge.¹⁵ Recently, computational models have also been employed to investigate the nanobio interactions at the molecular level. However, the complexity of the systems limits the results on the protein conformation¹¹ and the interactions with a simplified cell membrane model.¹⁶ Both computer

Received: June 5, 2013

Revised: August 1, 2013

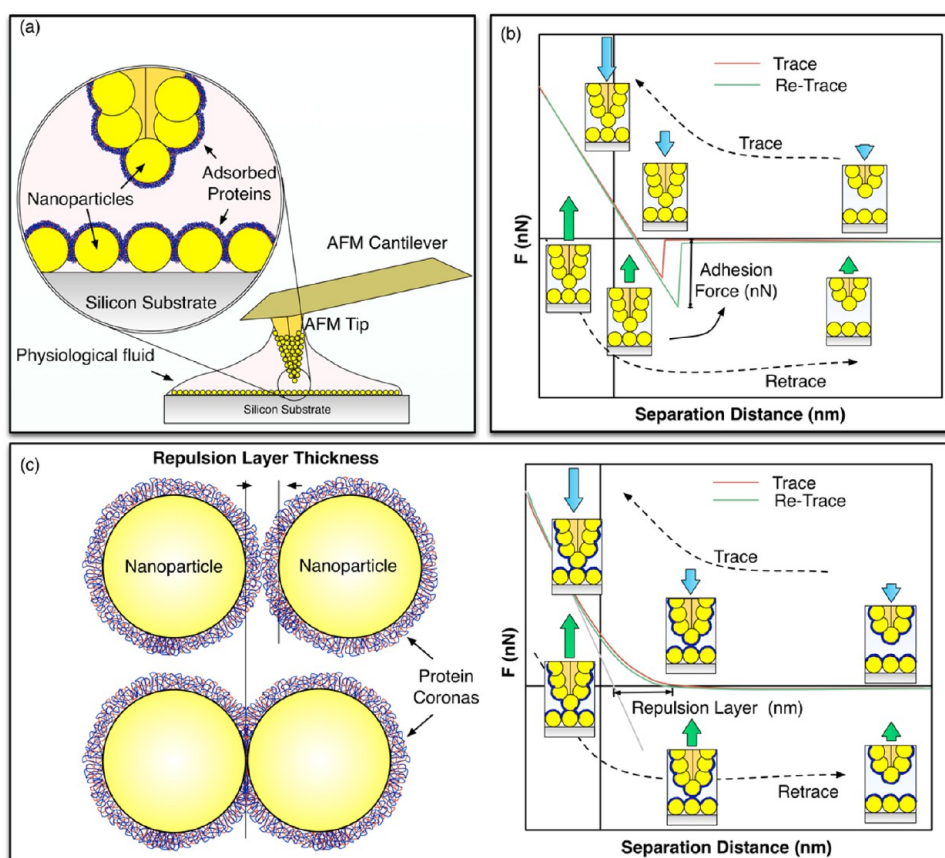


Figure 1. AFM apparatus and typical atomic force curves: (a) Illustration showcasing the direct force measurement apparatus. (b) In the case where the nanoparticles agglomerate, there is strong adhesion force indicated by the force required to pull the tip away from the surface. (c) In the case that the protein corona is present, there is a strong repulsion between the particles starting the moment the two coronas are brought in contact until they are fully compressed. The pictorial indicates the physical meaning of the RLT and its relation to the protein corona thickness.

simulations and proteomics analysis have clearly underlined the link between particle properties and composition/structure of the protein corona. Nevertheless, currently the interactions are experimentally assessed indirectly with techniques such as dynamic light scattering (DLS) that measures the particle agglomeration state, proteomics analysis that measures preferential protein adsorption, ellipsometry, and quartz microbalance that measures adsorbed amount. Although DLS data are valuable and insightful, they rely on numerous assumptions for the nature of the particles (spherical shape, uniform optical properties) and require accurate measurement of the indexes of refraction for both media and particles. These values are not readily available for all materials, thus adding an extra layer of assumptions. Similarly, proteomics analysis, ellipsometry, and quartz microbalance can differentiate and quantify the various proteins adsorbed on the particles, but cannot give information on specific nanoparticle–nanoparticle interactions.

Herein, we present one of the first attempts to assess the link of protein corona to the nanoparticle properties by measuring the atomic force between industry-relevant nanoparticles of controlled size suspended in physiological fluids. AFM is a state-of-the-art surface sensitive technique that has the ability to quantitatively and qualitatively characterize the interaction forces at molecular level. While it has been used extensively in material science for imaging¹⁷ and atomic force measurements,¹⁸ only recently has AFM been used for understanding nanobio interactions at the molecular level.¹⁹

Research Strategy. The overall research strategy is illustrated in Figure 1a. Nanoparticles with closely controlled properties were synthesized and attached on the AFM tip and also deposited in situ on Si substrate as explained in detail in the Materials and Methods. The nanoparticles were synthesized using the state-of-the-art Harvard Versatile Engineer Nanomaterial Generation System (VENGES).²⁰ VENGES is based on flame aerosol technology,²¹ which is widely used in the synthesis of particulate commodities (carbon black, pigmentary titania, and fumed silica) as well as novel sophisticated materials such as catalysts, gas sensors, biomaterials, and even nutritional products.²²

Two nanoparticle systems were used as test materials: CeO₂ and Fe₂O₃. Silica (SiO₂) was used as a control material. Cerium oxide is used extensively in many industrial and commercial applications, as catalyst,²³ additive in fuels,²⁴ oxygen storage in fuel cells,²⁵ pigment in cosmetics,²⁶ or abrasive medium in chemical mechanical polishing (CMP).²⁷ Although it is generally considered a nontoxic material, recent evidence suggests that in the nanoparticle form there might be adverse health effects²⁸ and environmental implications.²⁹ Iron oxide is widely utilized as pigment³⁰ and has recently attracted considerable attention due to its promising potential in biomedics for its superparamagnetic properties¹⁰ and in nutritional applications as food fortificant against anemia. Silica is widely accepted as a control for toxicological studies,^{28,32} and its interactions with various proteins have been studied in depth.³³

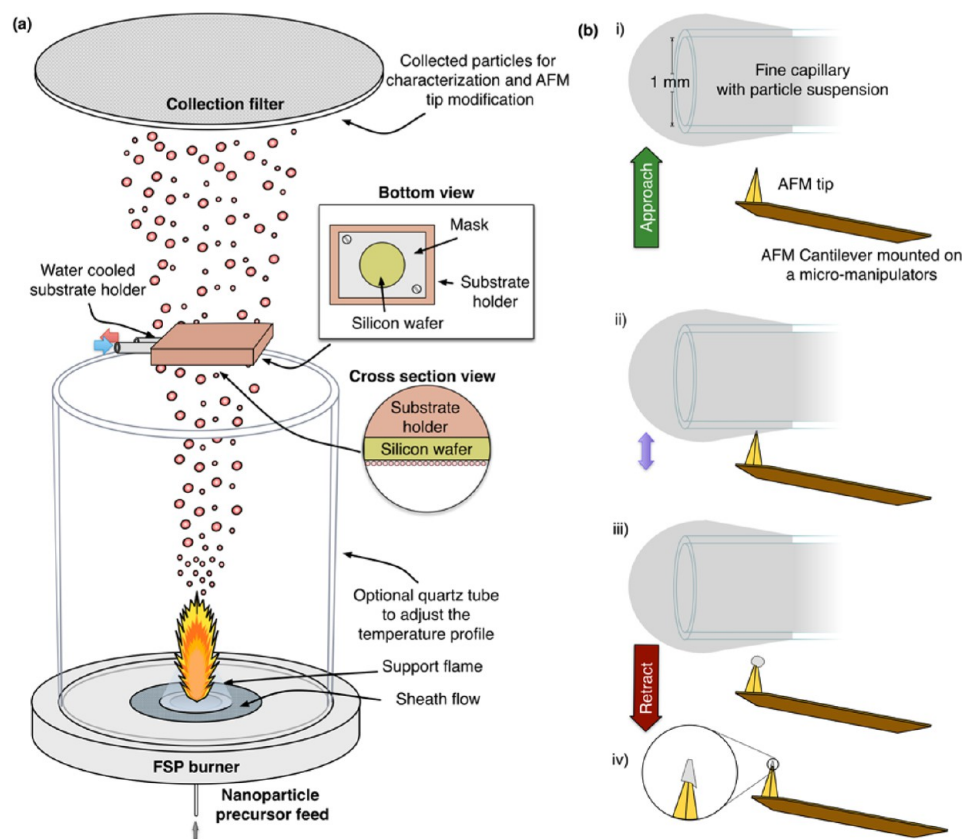


Figure 2. The process of producing the substrates and the nanoparticle attachment on the AFM tips. (a) The substrates are produced by direct deposition of the particles by FSP system. (b) The attachment of the nanoparticles on the tip. (i) The tips are coated with the creation of a fine droplet on the edge of a fine capillary. (ii) The tip is brought in contact with the created droplet and is dunked several times. (iii) A micro-sized droplet is formed at the edge of the tip. (iv) The droplet is left to dry to create a small particle aggregate.

The interaction force profile was measured between the nanoparticle coated tips and substrates for various biological media by AFM. As biological media, water, RPMI 1640 (Roswell Park Memorial Institute formulation 1640, referred to from now on as RPMI), and RPMI+10% FBS (Fetal Bovine Serum) were used. The aforementioned media are used extensively in the preparation of nanoparticle suspensions in toxicological studies.¹³

AFM measures the interaction force in two subsequent modes: (1) while the tip is approaching the surface (trace), and (2) when the tip is retreating away from the surface (retrace).³⁴ Typically, the atomic force is obtained as a function of the distance between AFM tip and substrate for both modes. Two important parameters were obtained from the AFM measurements: agglomeration potential and repulsion layer thickness. **Agglomeration Potential.** During the retrace mode, the “adhesion force” can be measured (Figure 1b). This force represents the nanoparticle’s potential to form agglomerates in the media with greater force translating to a greater tendency to agglomerate and remain agglomerated.

Repulsion Layer Thickness (RLT). When particles are suspended in physiological media, a protein corona forms that results in a repulsive force due to steric hindrance.³⁵ Therefore, when the AFM tip is approaching the surface (trace mode), the protein coronas on nanoparticles will be compressed mutually when they come in contact. This will result in a sharp increase in the measured atomic force. When the coronas are fully compressed, protein-coated nanoparticles behave as hard spheres. The interaction force increases linearly

with increasing distance as the particles are pushed together (Figure 1c). The distance from when the two coronas start to experience the repulsion force, and the point where their interaction assimilates that of hard spheres, is defined as the “repulsion layer thickness (RLT)” (Figure 1c).

The RLT indicates the magnitude of the repulsive force, where a larger RLT indicates a more effective stabilization of the nanoparticles in the physiological media. Although this behavior can be a characteristic of all kinds of repulsive forces (electrostatic, electrosteric, steric, etc.), for proteins the RLT is directly related to the corona thickness with RLT roughly twice the corona thickness (to account for two approaching particles as is illustrated in Figure 1c).

MATERIALS AND METHODS

The developed methodology has three major components: the particle synthesis and characterization, the attachment of nanoparticle on the AFM tips and substrates, and the direct atomic force profile measurement using AFM.

Synthesis of Nanoparticles. The nanoparticles were made by the flame spray pyrolysis (FSP)³⁶-based Harvard Versatile Engineer Nanomaterial Generation System (VENGES).^{20,28,37} Flame aerosol technology accounts for more than 90% of the total volume and value of nanostructured particle commodities produced in the gas-phase worldwide.³⁸ The advantages of this method include its precise control of the nanoparticles properties (i.e., composition, dimensions, shape, etc.), high yield (gr/h), and reproducibility.²² In contrast to other methods for producing nanoparticles, such as sol–gel and hydrothermal, flame aerosol technology at high oxidation conditions

generates nanoparticles free of organic residue³⁹ on their surface that can interfere with the toxicity or protein adsorption.

A precursor solution, which contains dissolved organometallic compounds in a high enthalpy solvent, is pumped through a stainless-steel capillary tube at a controlled flow rate. Oxygen flow disperses the liquid precursor solution into fine droplets, which are combusted by a small pilot flame. This results in the full conversion of the liquid precursor's organic constituents into metal oxide nanoparticles. The nanoparticle diameter is fully controlled by the operational parameters, and the results are consistent and reproducible.³⁶ The nanoparticles are collected on a water-cooled glass fiber filter (Whatmann, 25.5 cm Ø) for further use and off-line characterization. The whole flame-spray setup is depicted in Figure 2a.

For each nanoparticle, a specific liquid precursor has to be prepared. Different operational parameters were selected to accommodate the requirement of the different diameters.

CeO₂ Synthesis. For the CeO₂ nanoparticles, a precursor consisting of Ce(III) 2-ethylhexanoate in 2-ethylhexanoic acid (Alfa Aesar, 12% Ce) and *o*-xylene (EMD, >98%) at either 0.2 or 0.4 M Ce metal ions was used depending on the desired particle diameter. The pilot flame was kept identical for each synthesis method at a flow rate of 1.5 L/min CH₄ and 3.2 L/min O₂. For the CeO₂ (S), the 0.2 M ceria precursor was injected at 3 mL/min and dispersed with O₂ at 3 L/min.⁴⁰ For the CeO₂ (M), the 0.4 M precursor was injected at 8 mL/min and dispersed with 3 L/min of O₂. The CeO₂ (L) was also synthesized with the 0.4 M precursor, but was injected into an enclosed reactor consisting of a 40 cm long (49 mm Ø) quartz tube and sheathed by an additional 40 L/min oxygen flow. The precursor was injected at 5 mL/min and dispersed by 5 L/min of O₂. To quickly achieve a steady state of particle synthesis for the enclosed system, the quartz tube was preheated in a proceeding step, where the synthesis conditions were applied for a pure xylene precursor for 2 min.

Fe₂O₃ Synthesis. Fe₂O₃ nanoparticles synthesis was done with a 0.34 M precursor containing Fe(III) acetylacetonate (Aldrich, > 97%) in a *o*-xylene:acetonitrile (Sigma-Aldrich, >99.5%), 3:1 volume ratio, solvent mixture.⁴¹ For the Fe₂O₃, the enclosure was used for all diameters of nanoparticles. For the Fe₂O₃ (S), the precursor was fed at 5 mL/min with 5 L/min dispersion and 5 L/min sheath oxygen.⁴¹ The same precursor was also applied to generate the Fe₂O₃ (M) nanoparticles, one of which was synthesized with a 12 mL/min precursor and 3 L/min oxygen flow. For Fe₂O₃ (L), the precursor was injected at 8 mL/min and dispersed by 5 L/min of oxygen into an enclosed reactor (40 cm long, 49 mm Ø, quartz tube). Fifteen L/min of oxygen sheath gas was applied.⁴¹

SiO₂ Synthesis. The reference material, SiO₂, was synthesized with a 0.5 M Si precursor made of hexamethyldisiloxane (HMDSO, Fluka Analytical, > 98.5%) and ethyl alcohol pure (EMD, 200 Proof, >99.5%). Silica synthesis was done with a 6 mL/min precursor and 4 L/min dispersion O₂ flow rate.³⁷

The synthesis conditions are summarized in the Supporting Information (Table S-I). For all synthesis methods, the backpressure of the dispersion oxygen was regulated to 1.5 bar.

Nanoparticle Dispersion Preparation. The nanoparticle dispersions in water were prepared according to the protocol developed by Cohen et al.,¹³ which includes calibration of sonication equipment to ensure accurate application of delivered sonication energy (DSE) in J/mL.⁴² According to the protocol, to achieve stable suspensions over time with narrow particle size distribution, the delivered sonication energy (DSE) should exceed a critical value (DSE_{cr}). The DSE_{cr} for various materials have been previously experimentally determined, and the values varied from 161 to 242 J/mL.¹³ The required sonication was done with a Branson Sonifier S-450A (Branson Ultrasonics, Danbury, CT) fitted with a 3 in. cup horn (maximum power output of 400 W at 60 Hz, continuous mode, output level 3). For all applications in this study, 5 mL of nanoparticle suspensions was prepared at 1 mg/mL and sonicated for 10 min.

Nanoparticle Characterization. The nanoparticles were characterized with a transmission electron microscope (TEM) in regards to their diameter and shape with X-ray diffraction (XRD) regarding their crystal structure, with BET N₂-adsorption regarding their surface area.

Dynamic light scattering (DLS) was also used for agglomeration and surface charge characterization in liquid suspensions.

TEM. Nanoparticle dispersions were prepared as described before. After sonication, the nanoparticles suspension was diluted down to 100 µg/mL. TEM grids (Ted Pella Inc., Redding, CA) were submerged in the solution and allowed to dry. The particles were imaged with the Libra 120 (Carl, Zeiss Oberkochen, Germany).

XRD. The X-ray diffraction pattern was measured from 2θ 15–70° with a Bruker AXS D8 Advance (Bruker, Karlsruhe, Germany). The analysis of the diffraction spectrum was done with the instrument software (Topas 4 software, Bruker, Karlsruhe, Germany) using a Rietveld method to determine the nanoparticle phase and crystalline size.

DLS. The Malvern Nanosizer (Malvern, Worcestershire, United Kingdom) was used to determine the zeta potential and hydrodynamic diameter of the nanoparticle liquid suspensions. Suspensions of 0.1 mg/mL were prepared from the stock dispersions, produced as described previously. The dependency of the nanoparticle's zeta potential on the pH in water was investigated by autotitration with MPT-2 Autotitrator (Malvern, Worcestershire, United Kingdom) from pH 4 to 9. The pH was adjusted with 0.1 M sodium hydroxide and 0.1 M hydrochloric acid.

Specific Surface Area. BET N₂-adsorption of the nanoparticles allowed for the determination of the specific surface area. Approximately 100–200 mg of the nanoparticle was flushed with a N₂ gas at 150 °C for >1 h with the Flow Prep 060 (Micromeritics, Norcross, GA). The specific surface area was measured with the TriStar (Micromeritics, Norcross, GA). The BET equivalent nanoparticle diameter (*d*_{BET}) was estimated under the assumption of spherical, monodispersed, nonagglomerated nanoparticles with:

$$d_{\text{BET}} = \frac{6000}{\text{SSA} \cdot \rho}$$

where the SSA is in m²/g, ρ is the material density in g/cm³, and *d*_{BET} is in nm.

Deposition of Nanoparticles on the Substrates. Two different approaches were followed in terms of preparing the nanoparticle films for the study: (1) direct particle deposition;⁴³ and (2) by utilizing a nanoparticle suspension (described in the Supporting Information).¹⁹

The utilized VENGES platform expedites the preparation of the substrates by directly exposing the Si substrates to the nanoparticle stream during the nanoparticle synthesis (Figure 2a, Materials and Methods).⁴³ The particles are deposited and adhered on the substrates without any additional aid. For the direct particle deposition on silicon wafer, the silicon wafer chip (<111> orientation, 5 × 5 mm chip, Ted Pella Inc., Redding, CA) was fixed onto a water-cooled substrate holder, and placed facing downward between the particle flame and the glass fiber filter (Figure 2a). The substrates were fixed at 40 cm above the FSP nozzle for all open flame synthesis procedures with the exception of the enclosed CeO₂ and Fe₂O₃ synthesis where the substrate height was set to 55.5 cm to accommodate the quartz tubes.

The particle morphology and yield are not stable during the first 10 s of the procedure and during the shutdown process. Therefore, during start up and shut down of the particle flame, the substrates were kept covered by a steel shield.⁴³ The shield was removed for the desired deposition duration (10–120 s) (the experimental conditions for the substrate manufacturing are summarized in the Supporting Information, Table S-I). The exposed time was optimized for each material and each particle diameter based on the surface coverage. The time for proper film formation was optimized for each case to yield a uniform continuous nanoparticle layer (Supporting Information, Figures S1–S3). Subsequently, the substrates were rinsed with ethanol to remove loosely attached particles.

The substrates were characterized regarding the utilized nanoparticle diameter and the overall nanoparticle film morphology and cohesion by scanning electron microscopy (Zeiss Ultra Plus, 2 kV) and atomic force microscopy (AFM, Asylum Research, Santa Clara, CA).

Nanoparticle Attachment on the AFM Tips. The tips, due to their very sensitive nature and small dimensions, cannot be directly

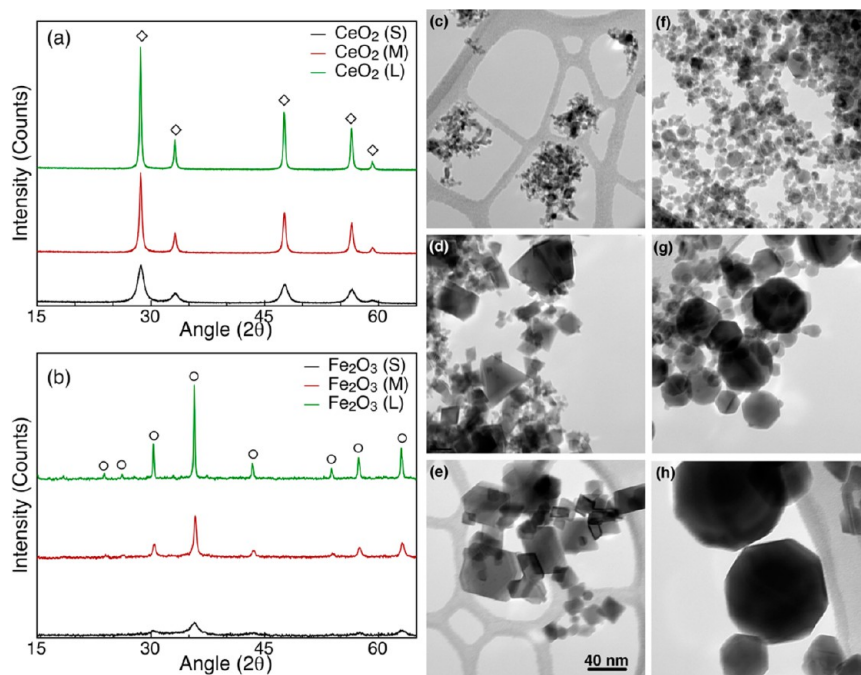


Figure 3. Structural characterization of the synthesized materials. XRD patterns of (a) cerium oxide and (b) iron oxide. TEM images of (c) $\text{CeO}_2(\text{S})$, (d) $\text{CeO}_2(\text{M})$, (e) $\text{CeO}_2(\text{L})$, (f) $\text{Fe}_2\text{O}_3(\text{S})$, (g) $\text{Fe}_2\text{O}_3(\text{M})$, and (h) $\text{Fe}_2\text{O}_3(\text{L})$, where L, M, and S correspond to the large (50–100 nm), medium (10–20 nm), and small (5–10 nm) sized ranges. The scale bar is the same for all images.

exposed to the high temperature of the FSP reactor. Instead, the nanoparticles were ex situ attached on the tips from aqueous suspensions with a modification of the method developed by Ong et al.⁴⁴

The nanoparticles were attached on the AFM cantilever tips (AC240TS, Olympus, Tokyo, Japan) with a fine coordination of Leica micromanipulators (Micromanipulator L, Leica Microsystems, Buffalo Grove, IL) under an inverted microscope (Leica DMIRB, Leica Microsystems, Buffalo Grove, IL) with a 20 \times magnification lens. The AFM cantilever tip was brought into the vicinity of a flint glass capillary tube (VWR, Radnor, PA) previously filled with the desired nanoparticle aqueous dispersion. A small dispersion droplet was ejected from the capillary and carefully allowed to circulate the first 5 mm of the outside cylindrical surface of the capillary tip for about 2 min to evenly wet the capillary front. The tip was then slowly brought into contact with the remaining dispersion for 15–30 touch intervals. Subsequently, the AFM tips were allowed to dry at ambient room condition. Figure 2b summarizes this procedure.

The tips were used in the following order: (i) air; (ii) water; (iii) RPMI; and (iv) RPMI+10%FBS.

Force Measurements Using AFM. The forces are obtained and presented as a function of the distance between the substrate and the tip. The force curves were obtained in four different environments: (i) air, (ii) DI water, (iii) RPMI, and (iv) RPMI+10% Fetal Bovine Serum (FBS). All of the measurements were conducted with the Asylum MFP-3D AFM System (Asylum Research, Santa Barbara, CA) sitting on a TS-150 vibration isolation table (Asylum Research, Santa Barbara, CA) and enclosed in AEK 2002 acoustic isolation enclosure (Asylum Research, Santa Barbara, CA).

All of the nanoparticle-coated substrates were fixed on glass slide with Crystalbond 509 adhesive (Ted Pella Inc., Redding, CA). The slide was heated on a hot plate at 150 $^{\circ}\text{C}$. The adhesive stick was brought in contact with the hot glass slide, and a small portion was melted on the slide glass. The substrate was immediately placed on the adhesive parallel to the glass slide with tweezers and was allowed to cool.

No additional instruments were required for the liquid measurements as they were executed by forming a liquid meniscus between the AFM tip holder and the substrate (Figure 1a). The substrate and the

AFM tips were left in the utilized media for 1 h so the system would come to equilibrium.

AFM Tip Spring Constant Measurement. The spring constant of the AFM tips was measured with the nanoparticles attached to account for the added mass of the particles and the corresponding change to the resonance frequency. It was experimentally determined in air over a mica surface according to the standardized protocol developed by Torii et al.⁴⁵

Force Measurement Protocol and Statistics. The surface of the substrate was imaged in AC (noncontact) mode prior to force measurements, to identify the nanoparticle location for the force measurements. By using the built-in software (Asylum Research, Santa Clara, CA), 10–15 sampling points, based on the morphology of the scanning area, were chosen systematically and were well distributed prior to force measurements.

The used tips were examined by SEM before and after each use to verify the adherence of the nanoparticles to the tip and therefore also the validity of the measured forces.

Statistics. In each location was a minimum of 20 consecutive extension/retraction movements resulting in more than 200 force curves for each case in each medium. The forces acting between the substrate and tip were measured in contact mode. Several pairs of substrates and tips were used for each case. The standard deviation for the error bar was used as the error in the calculation of both the RLT and the adhesion force.

Force Analysis. The force curves were processed, and the calculation of adhesion force and RLT was done with an in-house developed Mathematica algorithm (Wolfram Research, Somerville, MA). The AFM gives the force as a function of the tip displacement and not directly as a function of the surface tip distance. This results in force curves that are not aligned. Therefore, before averaging the measured force plots, they were shifted so that at large separation distance ($\sim 1\ \mu\text{m}$) there is zero net force (shift along y axis). For the adhesion force, the force curves were shifted across the x-axis to align the minima at $x = 0\ \text{nm}$. For the case of repulsion, the curves were shifted to align linear portion of the curves (shift along the x axis). The RLT and the adhesion force were calculated individually from each curve. The obtained values were averaged, and the standard deviation was used as the error. Outliers control removed values that are outside

Table 1. BET Specific Surface Area, BET Calculated Diameter, XRD Particle Diameter, Hydrodynamic Diameter, and Zeta Potential in Water and RPMI+10%FBS, for All of the Nanoparticles Investigated in This Study^a

NP ref name	SSA [m ² /g]	d_{BET} [nm]	d_{XRD} [nm]	hydrodynamic diameter (pH) [mV]		zeta potential [mV]	
				water	cell media	water	cell media
CeO ₂ (S)	144.5	5.4	10.6	254.7 ± 21.7 (6.1)	469.0 ± 124.6 (7.14)	5.2	−8.2
CeO ₂ (M)	53.8	14.6	27.2	108.0 ± 3.8 (6.1)	343.9 ± 52.4 (7.14)	2.2	−23.6
CeO ₂ (L)	25.9	30.3	45.9	140.8 ± 1.9 (6.4)	429.1 ± 3.8 (7.14)	10.2	−21.7
Fe ₂ O ₃ (S)	123.0	9.3	10.1	106.9 ± 6.9 (6.3)	335.2 ± 8.8 (7.14)	11.1	−10.3
Fe ₂ O ₃ (M)	54.7	20.9	24.5	237.2 ± 5.0 (6.4)	1219.0 ± 132.5 (7.14)	2.8	−8.62
Fe ₂ O ₃ (L)	13.7	83.4	90.6	6171.7 ± 1083 (6.5) ^c	4250.0 ± 94.9 (7.14)	−0.7	−8.81
SiO ₂	154.3	14.7	− ^b	129 ± 2.9 (6.6)	203.4 ± 11.2 (7.14)	−47.3	−16.6

^aThe value of d_{BET} is computed from the SSA and the corresponding material density under the assumption of spherical, monodispersed, non-agglomerated nanoparticles. ^bNo XRD size available for amorphous materials. ^cBecause of rapid sedimentation, value is susceptible to large error.

the range of $\pm 3\sigma$ (σ : standard deviation). Subsequently, the force curves were averaged and plotted.

RESULTS AND DISCUSSION

Particle Synthesis and Characterization. The CeO₂ and Fe₂O₃ nanoparticles were synthesized in three distinct primary particle (PP) diameters of 5–10, 20–50, and 50–100 nm denoted with S, M, and L, respectively. Additionally, SiO₂ nanoparticles, a reference material, were synthesized at a PP diameter of about 15 nm.

Figure 3 shows collectively the structural characterization of (a) CeO₂ and (b) Fe₂O₃ for all particle diameters. Figure 3c–h shows TEM images of these particles. Table 1 summarizes the PP diameter based on the XRD patterns (Rietveld analysis), the Brunauer–Emmett–Teller (BET) N₂ adsorption specific surface area, and the corresponding computed diameter.

The XRD patterns confirm the crystalline structure for both CeO₂ and Fe₂O₃. The CeO₂ nanoparticles are cubic (CaF₂ structural type), in agreement with the literature.³⁶ The Fe₂O₃ nanoparticles are gamma phase, in agreement again with FSP literature.⁴¹ Both the XRD patterns and the TEM images confirm the diameter variation and structure of the synthesized nanoparticles exhibiting the hexagonal form of the Fe₂O₃ particles⁴⁶ and the rhombohedral shape of the CeO₂ particles.³⁶ It is evident from the images that there is a nearly self-preserving diameter distribution that is common for flame generated materials.²¹ The images also demonstrate that the desired variation in diameter was achieved for both materials without altering the material phase, as seen from XRD (Figure 3a,b).

Nanoparticle Deposition on Substrates and AFM Tips.

Substrate Characterization. Figure 4 shows the AFM and SEM characterization of the nanoparticle substrates for Fe₂O₃(L), CeO₂(L), and SiO₂ nanoparticles (the remaining substrates are presented in the Supporting Information, Figures S1–S3). The films appear to be cohesive and uniform. It is evident that the deposited nanoparticles maintained all of their properties and features during deposition. This is confirmed by the AFM topography, which reveals that the curvature radius of particles on substrates is similar to the particles suspended in media. Maintaining the same features is critical because the particle curvature affects nanoparticle–protein interactions.⁴⁷

AFM Tips Characterization. Figure 5a–c shows the SEM imaging of the tips with the attached SiO₂, Fe₂O₃(L), and CeO₂(L) nanoparticles (all of the AFM tips are in the Supporting Information, Figure S5).

The SEM photograph series in Figure 5d–f shows an exemplary tip that has been used in a series of force

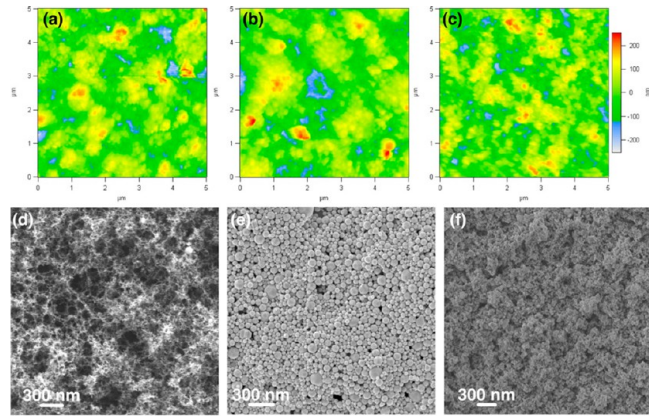


Figure 4. AFM topography of (a) SiO₂, (b) Fe₂O₃(L), and (c) CeO₂(L). The respective SEM images of (d) SiO₂, (e) Fe₂O₃(L), and (f) CeO₂(L).

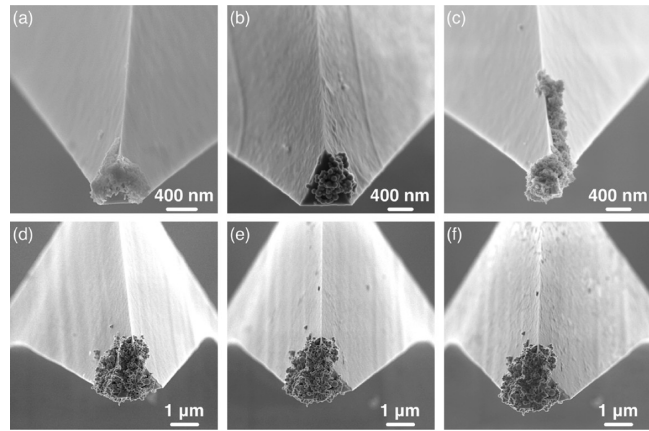


Figure 5. SEM images of the AFM tips with (a) SiO₂, (b) Fe₂O₃(L), and (c) CeO₂(L) attached. A freshly made AFM tip with the Fe₂O₃(L) nanoparticles attached: (d) unused, (e) after it was used in air to estimate the spring constant, and (f) after it has been used in RPMI and RPMI+10%FBS.

measurements with no apparent change in its morphology. This is clear evidence that attached particles remain stable on the tip. Figure 5d shows a tip coated with Fe₂O₃(L) prior to its use in AFM measurements. Figure 5e shows the same tip after being used for force measurements in two media (200 measurements in air and 200 measurements in water). The same tip is shown in Figure 5f after being used in consecutive measurements in two additional media (200 measurements in

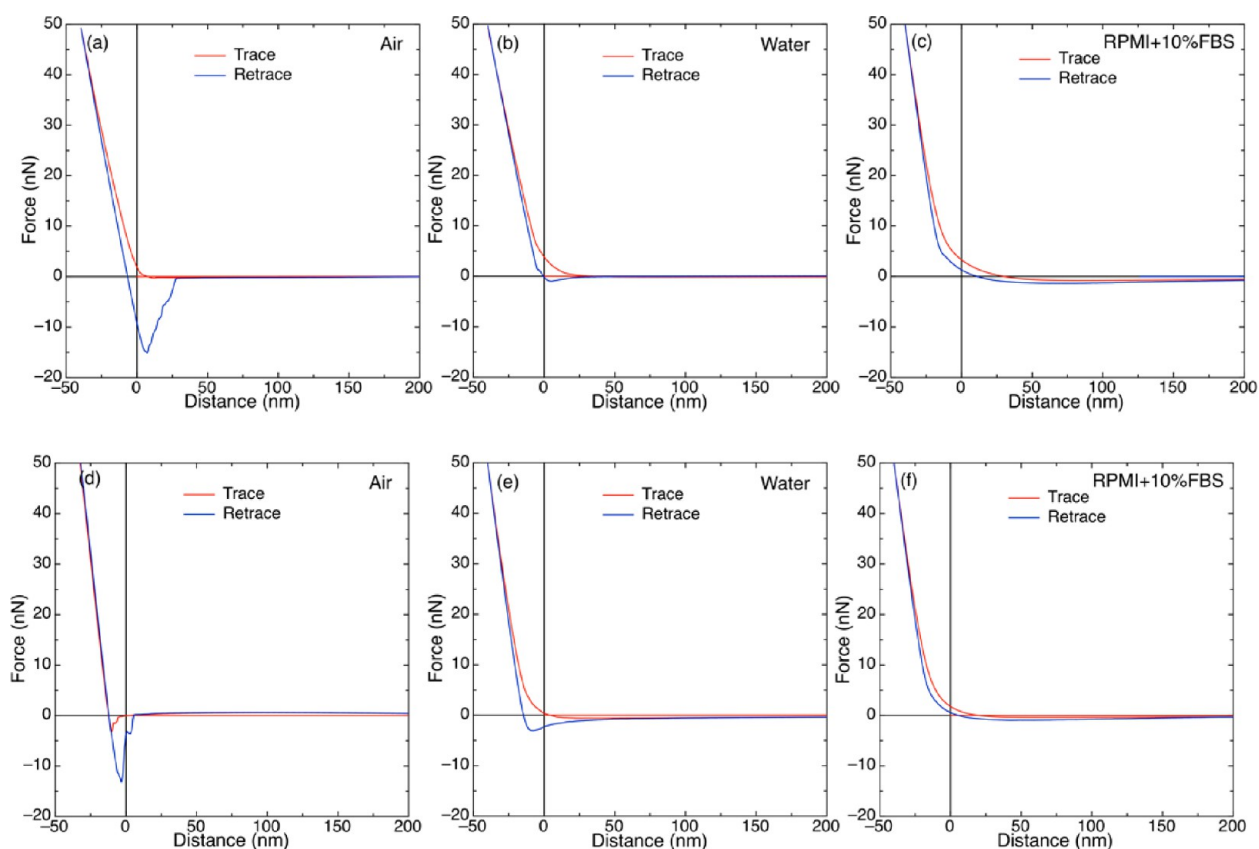


Figure 6. Representation of the averaged force curves. The AFM force measured for the CeO_2 in (a) air, (b) water, and (c) RPMI+10%FBS. Similarly, the AFM force measured for the Fe_2O_3 in (d) air, (e) water, and (f) RPMI+10%FBS.

449 RPMI and 200 measurements RPMI+10%FBS). It is clear that
450 nanoparticles attached to the tip as described adhere there
451 during multiple force measurements in consecutive media.

452 **Overall AFM Platform Quality Assessment.** In summary,
453 from the data presented in Figures 4 and 5, it is evident that the
454 developed methodology allows for the attachment of particles
455 while maintaining the same surface features of the single
456 particles. Moreover, the tips can be used repeatedly for force
457 measurements in various media without any apparent alteration
458 of their original properties. The particles remain at the location
459 where they were originally attached.

460 **Nanoparticle–Nanoparticle Interactions in Media.**
461 The nanoparticle–nanoparticle interactions were investigated
462 with two different methods: the dynamic light scattering (DLS)
463 and the direct nanoparticle–nanoparticle interaction utilizing
464 the proposed AFM-based approach.

465 **Characterization of the Nanoparticles in Media.** The
466 nanoparticles suspensions were characterized with DLS in
467 water and RPMI+10%FBS. Figure S6 in the Supporting
468 Information presents the DLS characterization data, including
469 the zeta potential measurements as a function of the pH in
470 water and the size distributions in water and RPMI+10%FBS.
471 The hydrodynamic diameter and zeta potential values in DI
472 water and RPMI+10%FBS are summarized in Table 1.

473 As shown in Table 1, the surface charge of the nanoparticles
474 is dependent upon the material and the PP diameter. The
475 isoelectric point (IEP) (Figure S6) for all nanoparticles is in
476 agreement with the literature (approximately 7 for CeO_2 ²⁷ and
477 Fe_2O_3 including FSP-made Fe_2O_3 ,⁴⁶ which is also approx-
478 imately 7). Silica is negatively charged in the entire evaluated
479 pH range in agreement with FSP-made silicas.³⁹ Also, in RPMI

+10%FBS the zeta potential is negative for all of the
nanoparticles, in good agreement with literature.⁴⁸

DLS also revealed that, in general, the nanoparticle
suspensions exhibit narrow size distributions, as demonstrated
by the low polydispersity indexes (0.163–0.459), except for
 $\text{Fe}_2\text{O}_3(\text{L})$ (polydispersity index of 0.672). More specifically, in
water, the agglomerates of CeO_2 nanoparticles have an average
hydrodynamic diameter between 150 and 250 nm regardless of
PP diameter. For the agglomerates of Fe_2O_3 nanoparticles in DI
water, there is a gradual increase in the hydrodynamic diameter
with constituent PP diameter. In particular, the $\text{Fe}_2\text{O}_3(\text{L})$
agglomerates appear to be quite polydisperse with an average
hydrodynamic diameter of approximately 6.1 μm . This is in
accordance with the zeta potential values that display a similarly
gradual decrease as a function of PP diameter. It should be
noted that for Fe_2O_3 the magnetic coercivity increases with
particle diameter of 20 nm and larger,⁴⁹ resulting in large
agglomerates that were also evident⁴⁶ for FSP-made uncoated
 Fe_2O_3 . These forces are long-range forces but are significantly
weaker than van der Waals in short-range, and, therefore, in this
study are not considered significant. The reference material,
silica, as expected, had a rather narrow agglomerate size
distribution in suspension in accordance with the literature.¹³

In the presence of FBS, all nanoparticle suspensions exhibit a
fairly narrow distribution of sizes, as indicated from their low
polydispersity index (0.217–0.423). This is in agreement with
the preparation protocol followed in this study that is designed
to produce nanoparticle suspensions with a narrow size
distribution.¹³ More specifically, in RPMI+10%FBS, the CeO_2
agglomerates have a hydrodynamic diameter of approximately 500
400 nm again regardless of PP diameter. On the contrary, for

the Fe_2O_3 , the hydrodynamic diameter increases with increasing PP diameter, although the zeta potential values remain approximately the same. Silica also appears narrowly distributed due to the high negative surface charge. The FBS adsorption on silica is limited,⁵⁰ and therefore there is a significant amount of free protein left in the solution that was measured by DLS (Supporting Information Figure S6e).

AFM Force Measurements. Figure 6 presents collectively the force as a function of distance for the case of SiO_2 , $\text{CeO}_2(\text{L})$, and $\text{Fe}_2\text{O}_3(\text{L})$, in suspension in different media. The obtained curves displayed in Figure 6 appear smooth, and the overall shape is similar to the theoretical shape described in Figure 1. The deviation from the average value was approximately 20% (maximum value was approximately 33%). The absence of the characteristic seesaw pattern⁵¹ indicates that the nanoparticles do not detach or shift in position during force measurements. Generally, it is observed that in both air and water there is a net attraction, while for RPMI+10%FBS there is a net steric repulsion, as expected.⁴ For each case, the magnitude varies on the basis of the nanoparticle material and medium. This is in agreement with literature data⁵² as these interactions depend both on the material's Hamaker constant (determining the attractive van der Waals forces) and on the structure of the corona, which depends on nanoparticle surface composition and diameter.⁴⁷

Figure 7 summarizes the AFM force results by focusing on the two metrics: the adhesion force and the repulsive layer thickness (RLT) for all nanoparticles. Silica is included as reference. Figure 7a and b shows the adhesion force for CeO_2 and Fe_2O_3 , respectively, in various media (air, water, RPMI, and RPMI+10%FBS). Figure 7c and d presents the RLT for the CeO_2 and Fe_2O_3 , respectively, in various media (air, water, RPMI, and RPMI+10%FBS). Figure 7e represents the dependence of the RLT on the PP size (XRD diameter) for both the CeO_2 and the Fe_2O_3 nanoparticles. Finally, Figure 7f shows the relation between the DLS measured hydrodynamic diameter and the RLT for all of the particles. The XRD measured PP size is indicated in the graph.

From air to water to RPMI, the adhesion is reduced for both nanoparticles. In air, the CeO_2 appears to have stronger adhesive forces than Fe_2O_3 , in agreement with the literature as CeO_2 has a larger Hamaker constant than Fe_2O_3 (5.56×10^{-20} vs 2.1×10^{-20} J, respectively).⁵³ In water, the magnitude of the attraction is reduced due to surface charges. However, because the pH is close to the IEP, the zeta potential has small values, and therefore the repulsion is not enough to entirely eliminate the adhesion. In RPMI, the magnitude of the interactions remains the same because there is only a small shift to the pH as compared to the DI water (from 6 to 7.41). In addition the small organic molecules present in RPMI adsorbed on the nanoparticle surface (sugars, vitamins, amino acids, etc.) cannot induce any significant changes (steric or electrostatic hindrance) due to their small sizes and charge. Moreover, the various electrolytes used to adjust the pH cannot effect the electrostatic interactions because the pH is already close to IEP. As expected, when the medium is RPMI+10%FBS, the adhesion potential completely diminishes for both the CeO_2 and the Fe_2O_3 . This is attributed directly to the protein corona formation and the corresponding steric stabilization it provides.⁵⁴ The reference material SiO_2 is well dispersed both in water and in RPMI+10%FBS, in alignment with the adhesion force data.

One of the most important results from the AFM force analysis is the dependence of adhesion force between the CeO_2

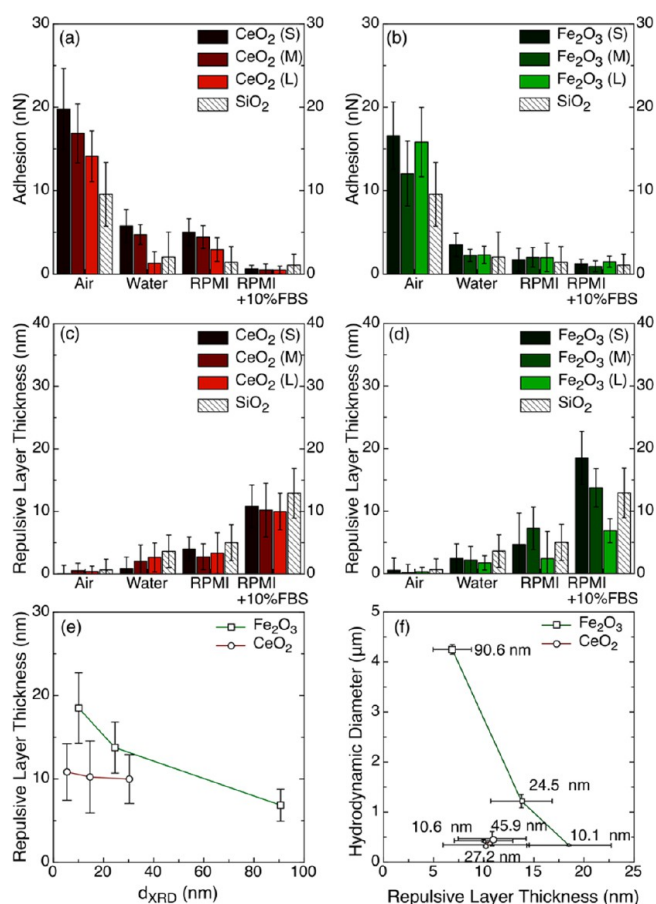


Figure 7. Collective representation of the AFM results. (a) The adhesion force between the CeO_2 nanoparticles and (b) Fe_2O_3 nanoparticles. (c) Similarly, the RLT for the CeO_2 nanoparticles and (d) Fe_2O_3 nanoparticles. (e) The repulsive layer thickness as a function of the primary particle size. (f) The relation between the hydrodynamic diameter and the RLT for all of the particles. The XRD measured PP size is indicated in the graph.

nanoparticles on particle diameter. This trend was not observed for Fe_2O_3 nanoparticles. These results indicate that the particle interactions in media are ambiguous processes that depend on the media particle diameter and composition.

For Fe_2O_3 nanoparticles, the corona thickness ($\sim 1/2$ RLT) depends on the PP diameter (Figure 7b). However, for the CeO_2 nanoparticles, the corona thickness does not seem to depend on the PP diameter (Figure 7e). The data are in agreement with the literature, which suggests that the protein corona formation depends both on the nanoparticle material and on the dimensions.⁵⁵ Moreover, when the RLTs are compared to the DLS measurements, it is evident that the differences in the protein corona thickness can be directly related to the dispersibility of the particles as indicated by the polydispersity index and hydrodynamic diameter. For the Fe_2O_3 nanoparticles, the RLT decreases when the PP diameter increases (Figure 7f). At the same time, the hydrodynamic diameter in RPMI+10%FBS increases, which indicates that the nanoparticles tend to agglomerate more. However, for the CeO_2 nanoparticles, both the hydrodynamic diameter and the RLT seem to be irrelevant to the PP diameter.

It is well established that a larger corona thickness (larger RLT) translates to more effective dispersibility because the particles are kept at larger separation distance and therefore do

not tend to agglomerate.⁵⁶ Thus, when the RLT of the Fe₂O₃ nanoparticles decreases, the particle dispersibility is reduced, resulting in larger agglomerates and a greater hydrodynamic diameter. On the contrary, CeO₂ has no variation in the RLT in respect to the PP diameter. Furthermore, the hydrodynamic diameter of the ceria has approximately the same value for all PP diameters. This is a clear indication that the particle properties impact the corona, and the corona in turn impacts the nanoparticle–nanoparticle interactions.

It is worth mentioning that the value of the RLT in RPMI +10%FBS is always within 12–36 nm, which represents a corona thickness between 6 and 18 nm. This is consistent with the dimension of the bovine serum albumin (4–14 nm),⁵⁷ which is the dominant protein in the solution (more than 99%). BSA is a globular protein that in physiological solutions has dimensions of 4 × 4 × 14 nm⁵⁸ and approximately 7 nm hydrodynamic diameter when measured with DLS.⁵⁹ Change in the conformation of the protein can result in different layer thicknesses ranging from 5 nm (smallest dimension of the BSA) to 15 nm (largest dimension).⁶⁰

The presented results demonstrate the high specificity of the nanoparticle–nanoparticle interactions and the thickness of the formed corona. These interactions depend on the material, the primary particle size, and the physiological media. Currently, these interactions are only investigated with computer simulations¹¹ and proteomics analysis.¹⁵ Here, we presented one of the first attempts to directly assess them experimentally. Although in the presented work we used the RPMI and the RPMI+10%FBS, both relevant to in vitro toxicology studies, the technique is not limited to these media/fluids. Every physiological medium that is optically transparent enough so it does not obstruct the AFM laser can be used. Such fluids can be physiological fluids like lung lining fluids, surfactant layer in the airways, mucus layer, etc. Additionally, the developed methodology can also be used effectively with any other nanomaterial that can be attached on the AFM tip, allowing one to investigate a large number of potential interactions.

CONCLUSIONS

This study is one of the first attempts to assess the nature and quantify the magnitude of the nanoparticle–nanoparticle interactions in physiological media using atomic force microscopy. We presented the required methodology to directly measure the atomic forces that determine these interactions in physiological media. The presented AFM approach has some major advantages over indirect methods like DLS, proteomics, or computer simulations. It is a bottom-up approach that can directly assess these interactions without any of the limitations the aforementioned techniques have. This method provides an extra layer of information, in addition to the currently utilized methods (DLS, proteomics, and computer simulation), in an effort to understand the nanobio interactions with emphasis on the agglomeration potential of nanoparticles, their stability, and the thickness of the formed protein corona. In the future, the developed AFM platform will be used to investigate the forces between nanoparticles and cells. This will provide another layer of information and link the atomic forces to biological/toxicological properties of nanomaterials.

ASSOCIATED CONTENT

Supporting Information

Images of the substrates with the deposited nanoparticles, the AFM tips with the nanoparticles attachment for all cases, and

an alternative method for preparing the substrates. This material is available free of charge via the Internet at <http://pubs.acs.org>.

AUTHOR INFORMATION

Corresponding Author

*Tel.: 617-432-3481. E-mail: pdemokri@hsph.harvard.edu.

Notes

The authors declare no competing financial interest.

ACKNOWLEDGMENTS

We would like to acknowledge the Center for Nanotechnology and Nanotoxicology at the Harvard School of Public Health, the Harvard Career Incubator Fund, NSF grant no. 1235806, and the European Research Council under the European Union's Seventh Framework Program (FP7/2007-2013, ERC grant agreement no. 247283) for their financial support. We would also like to acknowledge Sandra Pirela for her assistance with the DLS measurements, Dr. Margaret Thompson, manager of the Transgenics laboratory at the Children's Hospital and Developmental Diabetes Research Center (Boston, MA), for providing the Leica micromanipulators, and the Center for Nanoscale Systems (CNS) at Harvard University, for the access and support of AFM, TEM, and SEM.

REFERENCES

- (1) Scheringer, M. Nanoecotoxicology: Environmental Risks of Nanomaterials. *Nat. Nanotechnol.* **2008**, *3*, 322–323.
- (2) Bello, D.; Martin, J.; Santeufemio, C.; Sun, Q.; Lee Bunker, K.; Shafer, M.; Demokritou, P. Physicochemical and Morphological Characterisation of Nanoparticles From Photocopiers: Implications for Environmental Health. *Nanotoxicology* **2012**.
- (3) Philbert, M. A.; Alexeeff, G. V.; Bahadori, T.; Balbus, J. M.; Bawendi, M. G.; Biswas, P.; Colvin, V.; Klaine, S. J.; Maynard, A. D.; Monteiro-Riviere, N. A.; Oberdörster, G.; Ratner, M. A.; Teeguarden, J. G.; Weisner, M. *Review of Federal Strategy for Nanotechnology-Related Environmental, Health, and Safety Research*; The National Academic Press: Washington, DC, 2008; pp 1–131.
- (4) Nel, A. E.; Mädler, L.; Velegol, D.; Xia, T.; Hoek, E. M. V.; Somasundaran, P.; Klaessig, F.; Castranova, V.; Thompson, M. Understanding Biophysicochemical Interactions at the Nano-Bio Interface. *Nat. Mater.* **2009**, *8*, 543–557.
- (5) Melancon, M. P.; Zhou, M.; Li, C. Cancer Theranostics with Near-Infrared Light-Activatable Multimodal Nanoparticles. *Acc. Chem. Res.* **2011**, *44*, 947–956.
- (6) Grobmyer, S. R.; Morse, D. L.; Fletcher, B.; Gutwein, L. G.; Sharma, P.; Krishna, V.; Frost, S. C.; Moudgil, B. M.; Brown, S. C. *J. Surg. Oncol.* **2011**, *103*, 317–325.
- (7) Saraceno, R.; Chiricozzi, A.; Gabellini, M.; Chimenti, S. Emerging Applications of Nanomedicine in Dermatology. *Skin. Res. Technol.* **2013**, *19*, e13–9.
- (8) Bu, L.; Xie, J.; Chen, K.; Huang, J.; Aguilar, Z. P.; Wang, A.; Sun, K. W.; Chua, M.-S.; So, S.; Cheng, Z.; Eden, H. S.; Shen, B.; Chen, X. Assessment and Comparison of Magnetic Nanoparticles as MRI Contrast Agents in a Rodent Model of Human Hepatocellular Carcinoma. *Contrast Media Mol. Imaging* **2012**, *7*, 363–372.
- (9) Jain, K. K. Advances in the Field of Nanooncology. *BMC Med.* **2010**, *8*, 83.
- (10) Xi, L.; Grobmyer, S. R.; Zhou, G.; Qian, W.; Yang, L.; Jiang, H. Molecular Photoacoustic Tomography of Breast Cancer Using Receptor Targeted Magnetic Iron Oxide Nanoparticles as Contrast Agents. *J. Biophotonics* **2012**.
- (11) Lynch, I.; Dawson, K. A. Protein-Nanoparticle Interactions. *Nano Today* **2008**, *3*, 40–47.
- (12) DeLoid, G.; Cohen, J. M.; Darrah, T.; Pyrgiotakis, G.; Wohlleben, W.; Demokritou, P. Estimating Effective Density of

- 722 Engineered Nanomaterials for Accurate in Vitro Dosimetry. *ACS Nano*
723 **2013**, submitted.
- 724 (13) Cohen, J.; DeLoid, G.; Pyrgiotakis, G.; Demokritou, P.
725 Interactions of Engineered Nanomaterials in Physiological Media
726 and Implications for in Vitro Dosimetry. *Nanotoxicology* **2012**, 1–15.
- 727 (14) Cedervall, T.; Lynch, I.; Lindman, S.; Berggard, T.; Thulin, E.;
728 Nilsson, H.; Dawson, K.; Linse, S. Understanding the Nanoparticle-
729 Protein Corona Using Methods to Quantify Exchange Rates and
730 Affinities of Proteins for Nanoparticles. *Proc. Natl. Acad. Sci. U.S.A.*
731 **2007**, 104, 2050–2055.
- 732 (15) Wasdo, S. C.; Barber, D. S.; Denslow, N. D.; Powers, K. W.;
733 Palazuelos, M.; Stevens, S. M.; Moudgil, B. M.; Roberts, S. M.
734 Differential Binding of Serum Proteins to Nanoparticles. *Int. J.*
735 *Nanotechnol.* **2008**, 5, 92–115.
- 736 (16) Yang, K.; Ma, Y.-Q. Computer Simulation of the Translocation
737 of Nanoparticles with Different Shapes Across a Lipid Bilayer. *Nat.*
738 *Nanotechnol.* **2010**, 5, 579–583.
- 739 (17) Li, J.; Cassell, A.; Dai, H. Carbon Nanotubes as AFM Tips:
740 Measuring DNA Molecules at the Liquid/Solid Interface. *Surf.*
741 *Interface Anal.* **1999**, 28, 8–11.
- 742 (18) Rabinovich, Y. I.; Daosukho, S.; Byer, K. J.; El-Shall, H. E.;
743 Khan, S. R. Direct AFM Measurements of Adhesion Forces Between
744 Calcium Oxalate Monohydrate and Kidney Epithelial Cells in the
745 Presence of Ca^{2+} and Mg^{2+} Ions. *J. Colloid Interface Sci.* **2008**, 325,
746 594–601.
- 747 (19) Schaefer, J.; Schulze, C.; Marxer, E. E. J.; Schaefer, U. F.;
748 Wohlleben, W.; Bakowsky, U.; Lehr, C.-M. Atomic Force Microscopy
749 and Analytical Ultracentrifugation for Probing Nanomaterial Protein
750 Interactions. *ACS Nano* **2012**, 6, 4603–4614.
- 751 (20) Demokritou, P.; Büchel, R.; Molina, R. M.; Deloid, G. M.; Brain,
752 J. D.; Pratsinis, S. E. Development and Characterization of a Versatile
753 Engineered Nanomaterial Generation System (VENGES) Suitable for
754 Toxicological Studies. *Inhalation Toxicol.* **2010**, 22, 107–116.
- 755 (21) Pratsinis, S. E. Flame Aerosol Synthesis of Ceramic Powders.
756 *Prog. Energy Combust. Sci.* **1998**, 24, 197–219.
- 757 (22) Strobel, R.; Pratsinis, S. E. Flame Aerosol Synthesis of Smart
758 Nanostructured Materials. *J. Mater. Chem.* **2007**, 17, 4743–4756.
- 759 (23) Trovarelli, A. Catalytic Properties of Ceria and CeO_2 -
760 Containing Materials. *Catal. Rev.-Sci. Eng.* **1996**, 38, 439–520.
- 761 (24) Gorte, R. J. Ceria in Catalysis: From Automotive Applications to
762 the Water–Gas Shift Reaction. *AIChE J.* **2010**.
- 763 (25) Mai, H.-X.; Sun, L.-D.; Zhang, Y.-W.; Si, R.; Feng, W.; Zhang,
764 H.-P.; Liu, H.-C.; Yan, C.-H. Shape-Selective Synthesis and Oxygen
765 Storage Behavior of Ceria Nanopolyhedra, Nanorods, and Nanocubes.
766 *J. Phys. Chem. B* **2005**, 109, 24380–24385.
- 767 (26) Yabe, S.; Sato, T. Cerium Oxide for Sunscreen Cosmetics. *J.*
768 *Solid State Chem.* **2003**, 171, 7–11.
- 769 (27) Abiade, J. T.; Yeruva, S.; Choi, W.; Moudgil, B. M.; Kumar, D.;
770 Singh, R. K. Tribochemical Study of Ceria-Silica Interactions for CMP.
771 *J. Electrochem. Soc.* **2006**, 153, G1001.
- 772 (28) Demokritou, P.; Gass, S.; Pyrgiotakis, G.; Cohen, J. M.;
773 Goldsmith, W.; McKinney, W.; Frazer, D.; Ma, J.; Schwegler-Berry, D.;
774 Brain, J.; Castranova, V. An in Vivo and in Vitro Toxicological
775 Characterisation of Realistic Nanoscale CeO_2 Inhalation Exposures.
776 *Nanotoxicology* **2012**, 1–13.
- 777 (29) Zhang, H.; He, X.; Zhang, Z.; Zhang, P.; Li, Y.; Ma, Y.; Kuang,
778 Y.; Zhao, Y.; Chai, Z. Nano- CeO_2 Exhibits Adverse Effects at
779 Environmental Relevant Concentrations. *Environ. Sci. Technol.* **2011**,
780 45, 3725–3730.
- 781 (30) Tanner, A. O. Iron Oxide Pigments. *Minerals Yearbook*; U.S.
782 Geological Survey: Northborough, MA, 2011; Vol. 1, pp 1–7.
- 783 (31) Hilty, F. M.; Arnold, M.; Hilbe, M.; Teleki, A.; Knijnenburg, J.
784 T. N.; Ehrensperger, F.; Hurrell, R. F.; Pratsinis, S. E.; Langhans, W.;
785 Zimmermann, M. B. Iron From Nanocompounds Containing Iron and
786 Zinc Is Highly Bioavailable in Rats Without Tissue Accumulation.
787 *Nature* **2010**, 5, 374–380.
- 788 (32) Gass, S.; Cohen, J. M.; Pyrgiotakis, G.; Sotiriou, G. A.; Pratsinis,
789 S. E.; Demokritou, P. Safer Formulation Concept for Flame-Generated
790 Engineered Nanomaterials. *ACS Sustainable Chem. Eng.* **2013**.
- (33) Giacomelli, C.; Bremer, M.; Norde, W. ATR-FTIR Study of IgG
791 Adsorbed on Different Silica Surfaces. *J. Colloid Interface Sci.* **1999**,
792 220, 13–23.
- (34) Cappella, B.; Dietler, G. Force-Distance Curves by Atomic
794 Force Microscopy. *Surf. Sci. Rep.* **1999**, 34, 1–104.
- (35) Wells, M. A.; Abid, A.; Kennedy, I. M.; Barakat, A. I. Serum
796 Proteins Prevent Aggregation of Fe_2O_3 and ZnO Nanoparticles.
797 *Nanotoxicology* **2012**, 6, 837–846.
- (36) Mädler, L.; Stark, W. J.; Pratsinis, S. E. Flame-Made Ceria
799 Nanoparticles. *J. Mater. Res.* **2002**, 17, 1356–1362.
- (37) Sotiriou, G. A.; Diaz, E.; Long, M. S.; Godleski, J.; Brain, J.;
801 Pratsinis, S. E.; Demokritou, P. A Novel Platform for Pulmonary and
802 Cardiovascular Toxicological Characterization of Inhaled Engineered
803 Nanomaterials. *Nanotoxicology* **2011**.
- (38) Wegner, K.; Pratsinis, S. E. Scale-Up of Nanoparticle Synthesis
805 in Division Amie Reactors. *Chem. Eng. Sci.* **2003**, 58, 4581–4589.
- (39) Teleki, A.; Akhtar, M. K.; Pratsinis, S. E. The Quality of SiO_2 -
807 Coatings on Flame-Made TiO_2 -Based Nanoparticles. *J. Mater. Chem.*
808 **2008**, 18, 3547–3555.
- (40) Xia, T.; Kovochich, M.; Liong, M.; Mädler, L.; Gilbert, B.; Shi,
810 H.; Yeh, J. I.; Zink, J. I.; Nel, A. E. Comparison of the Mechanism of
811 Toxicity of Zinc Oxide and Cerium Oxide Nanoparticles Based on
812 Dissolution and Oxidative Stress Properties. *ACS Nano* **2008**, 2,
813 2121–2134.
- (41) Li, D.; Teoh, W. Y.; Selomulya, C.; Woodward, R. C.; Munroe,
815 P.; Amal, R. Insight Into Microstructural and Magnetic Properties of
816 Flame-Made Gamma- Fe_2O_3 Nanoparticles. *J. Mater. Chem.* **2007**, 17,
817 4876–4884.
- (42) Taurozzi, J. S.; Hackley, V. A.; Wiesner, M. R. Ultrasonic
819 Dispersion of Nanoparticles for Environmental, Health and Safety
820 Assessment—Issues and Recommendations. *Nanotoxicology* **2011**, 5,
821 711–729.
- (43) Mädler, L.; Roessler, A.; Pratsinis, S. E.; Sahm, T.; Gurlo, A.;
823 Barsan, N.; Weimar, U. Direct Formation of Highly Porous Gas-
824 Sensing Films by in Situ Thermophoretic Deposition of Flame-Made
825 Pt/ SnO_2 Nanoparticles. *Sens. Actuators, B* **2006**, 114, 283–295.
- (44) Ong, Q. K.; Sokolov, I. Attachment of Nanoparticles to the
827 AFM Tips for Direct Measurements of Interaction Between a Single
828 Nanoparticle and Surfaces. *J. Colloid Interface Sci.* **2007**, 310, 385–390.
- (45) Torii, A.; Sasaki, M.; Hane, K.; Okuma, S. A Method for
830 Determining the Spring Constant of Cantilevers for Atomic Force
831 Microscopy. *Europhys. Lett.* **1999**, 7, 179–184.
- (46) Teleki, A.; Suter, M.; Kidambi, P. R.; Ergeneman, O.; Krumeich,
833 F.; Nelson, B. J.; Pratsinis, S. E. Hermetically Coated Super-
834 paramagnetic Fe_3O_4 Particles with SiO_2 Nanofilms. *Chem. Mater.*
835 **2009**, 21, 2094–2100.
- (47) Lundqvist, M.; Sethson, I.; Jonsson, B. Protein Adsorption Onto
837 Silica Nanoparticles: Conformational Changes Depend on the
838 Particles' Curvature and the Protein Stability. *Langmuir* **2004**, 20,
839 10639–10647.
- (48) Maiorano, G.; Sabella, S.; Sorce, B.; Brunetti, V.; Malvindi, M.
841 A.; Cingolani, R.; Pompa, P. P. Effects of Cell Culture Media on the
842 Dynamic Formation of Protein–Nanoparticle Complexes and
843 Influence on the Cellular Response. *ACS Nano* **2010**, 4, 7481–7491.
- (49) Raming, T. P.; Winnubst, A. J. A.; van Kats, C. M.; Philipse, A.
845 P. The Synthesis and Magnetic Properties of Nanosized Hematite (α -
846 Fe_2O_3) Particles. *J. Colloid Interface Sci.* **2002**, 249, 346–350.
- (50) Larsericsdotter, H.; Oscarsson, S.; Buijs, J. Structure, Stability,
848 and Orientation of BSA Adsorbed to Silica. *J. Colloid Interface Sci.*
849 **2005**, 289, 26–35.
- (51) Salameh, S.; Schneider, J.; Laube, J.; Alessandrini, A.; Facci, P.;
851 Seo, J. W.; Ciacchi, L.; Mädler, L. Adhesion Mechanisms of the
852 Contact Interface of TiO_2 Nanoparticles in Films and Aggregates.
853 *Langmuir* **2012**.
- (52) Monopoli, M. P.; Bombelli, F. B.; Dawson, K. A. Nano-
855 biotechnology: Nanoparticle Coronas Take Shape. *Nat. Nanotechnol.*
856 **2011**, 6, 11–12.
- (53) Petosa, A. R.; Jaisi, D. P.; Quevedo, I. R.; Elimelech, M.;
858 Tufenkji, N. Aggregation and Deposition of Engineered Nanomaterials
859

- 860 in Aquatic Environments: Role of Physicochemical Interactions.
861 *Environ. Sci. Technol.* **2010**, *44*, 6532–6549.
- 862 (54) Lundqvist, M.; Stigler, J.; Elia, G.; Lynch, I.; Cedervall, T.;
863 Dawson, K. Nanoparticle Size and Surface Properties Determine the
864 Protein Corona with Possible Implications for Biological Impacts. *Proc.*
865 *Natl. Acad. Sci. U.S.A.* **2008**, *105*, 14265–14270.
- 866 (55) Monopoli, M. P.; Walczyk, D.; Campbell, A.; Elia, G.; Lynch, I.;
867 Baldelli Bombelli, F.; Dawson, K. A. Physical–Chemical Aspects of
868 Protein Corona: Relevance to in Vitro and in Vivo Biological Impacts
869 of Nanoparticles. *J. Am. Chem. Soc.* **2011**, *133*, 2525–2534.
- 870 (56) Lynch, I.; Cedervall, T.; Lundqvist, M.; Cabaleiro-Lago, C.;
871 Linse, S.; Dawson, K. A. The Nanoparticle–Protein Complex as a
872 Biological Entity; a Complex Fluids and Surface Science Challenge for
873 the 21st Century. *Adv. Colloid Interface Sci.* **2007**, *134–135*, 167–174.
- 874 (57) Wang, Y.; Wang, X.; Luo, G.; Dai, Y. Adsorption of Bovine
875 Serum Albumin (BSA) Onto the Magnetic Chitosan Nanoparticles
876 Prepared by a Microemulsion System. *Bioresour. Technol.* **2008**, *99*,
877 3881–3884.
- 878 (58) Wright, A. K.; T., M. R. Hydrodynamic Structure of Bovine
879 Serum Albumin Determined by Transient Electric Birefringence.
880 *Biophys. J.* **1975**, *15*, 137.
- 881 (59) Li, Y.; Yang, G.; Mei, Z. Spectroscopic and Dynamic Light
882 Scattering Studies of the Interaction Between Pterodonic Acid and
883 Bovine Serum Albumin. *Acta Pharm. Sin. B* **2012**, *2*, 53–59.
- 884 (60) van der Veen, M.; Stuart, M. C.; Norde, W. Spreading of
885 Proteins and Its Effect on Adsorption and Desorption Kinetics.
886 *Colloids Surf., B* **2007**, *54*, 136–142.